Supplemental Materials for Quantum squeezing in an all-resonant periodically poled lithium niobate microresonator

Xinyi Ren *et al.*

I. Fabrication process

Periodic poling and device fabrication were performed on 5 % MgO-doped, 600 nm-thick X-cut lithium-niobate-on-insulator wafers. Round-tip comb electrodes with a period of 4.742 µm were patterned by direct-write lithography, followed by electron-beam deposition of 10 nm Cr and 150 nm Au, and lift-off. A thick photoresist layer was applied to insulate the surface while leaving access windows above the electrode pads. High-voltage pulses of millisecond duration were then applied across the electrodes to pole the designated regions. The poling quality was verified using 2-photon microscopy, after which the electrodes were removed by sequential Au/Cr wet etching.

The poled wafers were subsequently patterned by electron-beam lithography with a thick hydrogen-silsesquioxane resist, and 350 nm of LN was etched by reactive-ion etching following established high-Q LN nanofabrication protocols. Following etching, the devices were cladded with plasma-enhanced chemical vapor deposition (PECVD) SiO_2 to suppress sidewall scattering and protect the surface. The chip was cleaved to form optical facets and subsequently coated with an additional PECVD oxide layer to serve as anti-reflection coatings and reduce facet reflection loss, as shown in Fig. 1**b**. The AR coating thickness was optimized to 270 nm for the FH wavelength (1560 nm), following the quarter-wave condition $d = \lambda/(4n_c)$, where n_c is the refractive index of the cladding. Finally, the chip was annealed at 500 °C for 5 h to improve oxide quality.

II. 2-photon imaging of periodically poled waveguide

We perform two-photon imaging using a Zeiss LSM 880 laser-scanning confocal microscope equipped with a Chameleon Ultra II Ti:Sapphire femtosecond laser. Imaging is repeated after full device fabrication to characterize the final duty cycle and poling depth. By extracting the intensity along the waveguide center and assigning intensity minima to the domain wall positions, we accurately determine the lengths of poled and unpoled sections (see Fig. S1). From the ratio of adjacent poled and unpoled section lengths, we obtain a duty cycle of 0.54 ± 0.01. Complete domain inversion through the lithium niobate film thickness is verified by comparing the peak intensity ratios between poled and unpoled regions.

III. Second-harmonic generation (SHG) characterization of microring resonator

We characterize the SHG using the setup shown in Fig. 2**a**. The FH light from a tunable near-infrared (NIR) laser (Santec TSL-570) is coupled into the microresonator through a lensed fiber, with its wavelength scanned from 1500–1630 nm. The generated SHG output at the visible wavelength is detected by a visible photodetector (PD, Thorlabs, APD120A), reflected after a long-pass dichroic mirror. When the input fundamental wavelength is tuned near 1587 nm, a strong SH peak emerges around 793.5 nm, confirming phase-matched conversion in the periodically poled section. The chip temperature is optimized to satisfy the co-resonance condition, and the maximum peak power within the visible band is selected from the measured SH spectrum. In the linear regime of the SHG process, the output SH power increased proportionally with the on-chip FH power. A normalized efficiency of 30 157 %/W is obtained from a linear fit, as shown in Fig. 2**d**.

IV. Co-resonance realization via precise temperature control

Owing to the different TO coefficients at the two wavelengths, co-resonance can be achieved by finely tuning the chip temperature within the QPM bandwidth. In the experiment, a NIR laser is used as the seed, and its SH is generated using an external SHG module. The NIR and visible transmissions are monitored simultaneously by separate

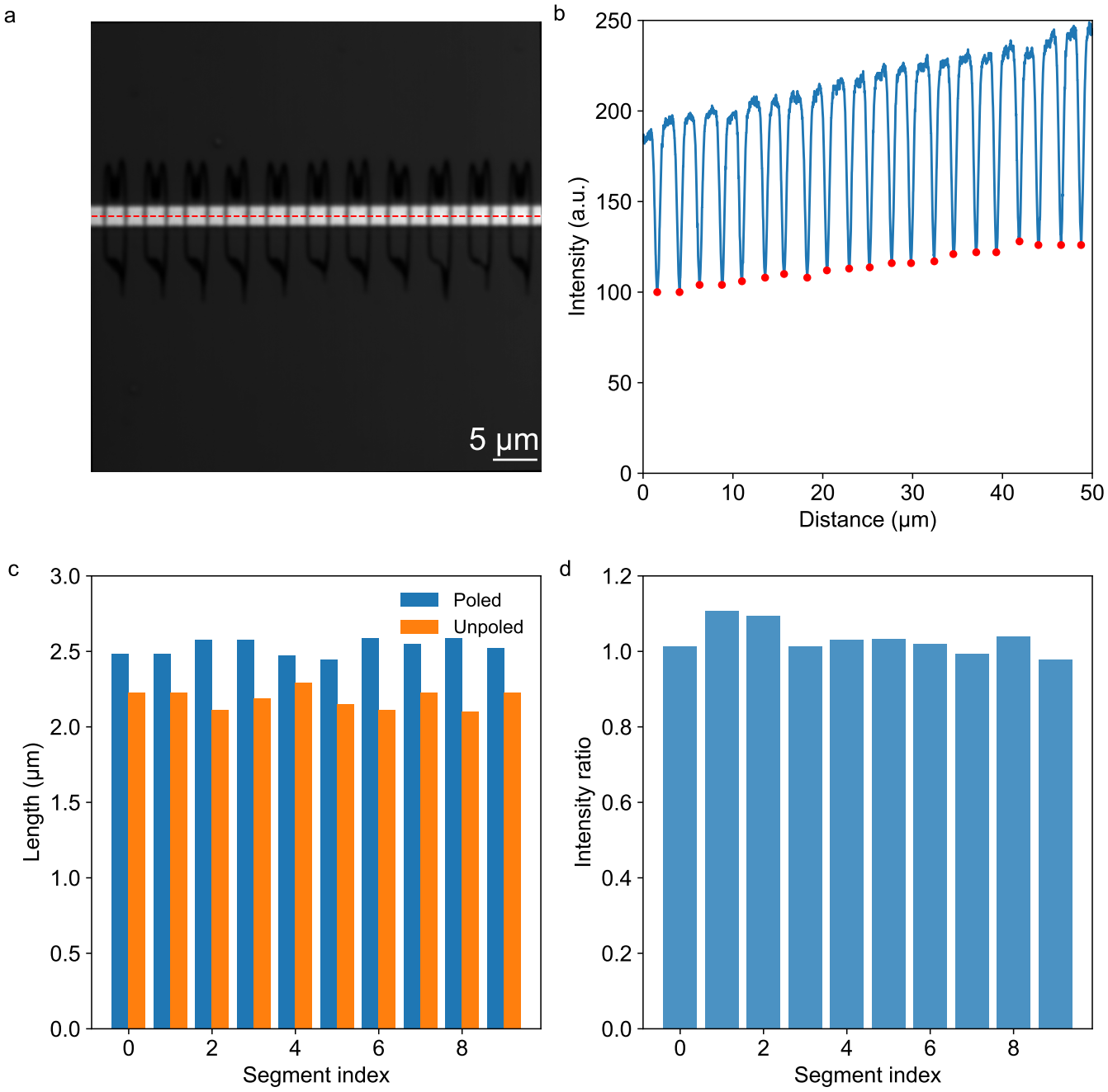

FIG. S1. **a**, 2-photon microscope image of a periodically poled waveguide. **b**, Intensity vs. distance plot along the red dotted line in (a). The red dots are the minima representing the domain wall positions. **c**, Length of poled and unpoled sections calculated from the domain wall positions. **d**, Peak intensity contrast of adjacent poled and unpoled sections.

photodetectors while the chip temperature is stabilized by a thermoelectric cooler (TEC), as shown in Fig. S2(a). The NIR wavelength is scanned by piezo tuning over a range of $\Delta\lambda$ of ≈ 40 pm, while the visible wavelength is tuned by $\Delta\lambda/2$ (Fig. S2(b)). The NIR transmission spectra under various temperatures are plotted in Fig. S2(c). As the temperature increases, the resonance positions of the two modes shift at different rates. Under certain temperature, they are optimally overlapping, leading to alternating amplification and de-amplification features when both modes coupled into the ring. The strongest modulation occurs near 62.847 °C, indicating the optimal co-resonant condition. Note that the relative detuning between the two wavelengths can also be extracted from their transmission spectra; however, this method is less sensitive than observing the amplitude and de-amplitude behavior because the strong

SH coupling in the cavity will affect the FH coupling due to instaous temperature change in the cavuity. This measurement is obtained using device 2, which will be discussed in the following section.

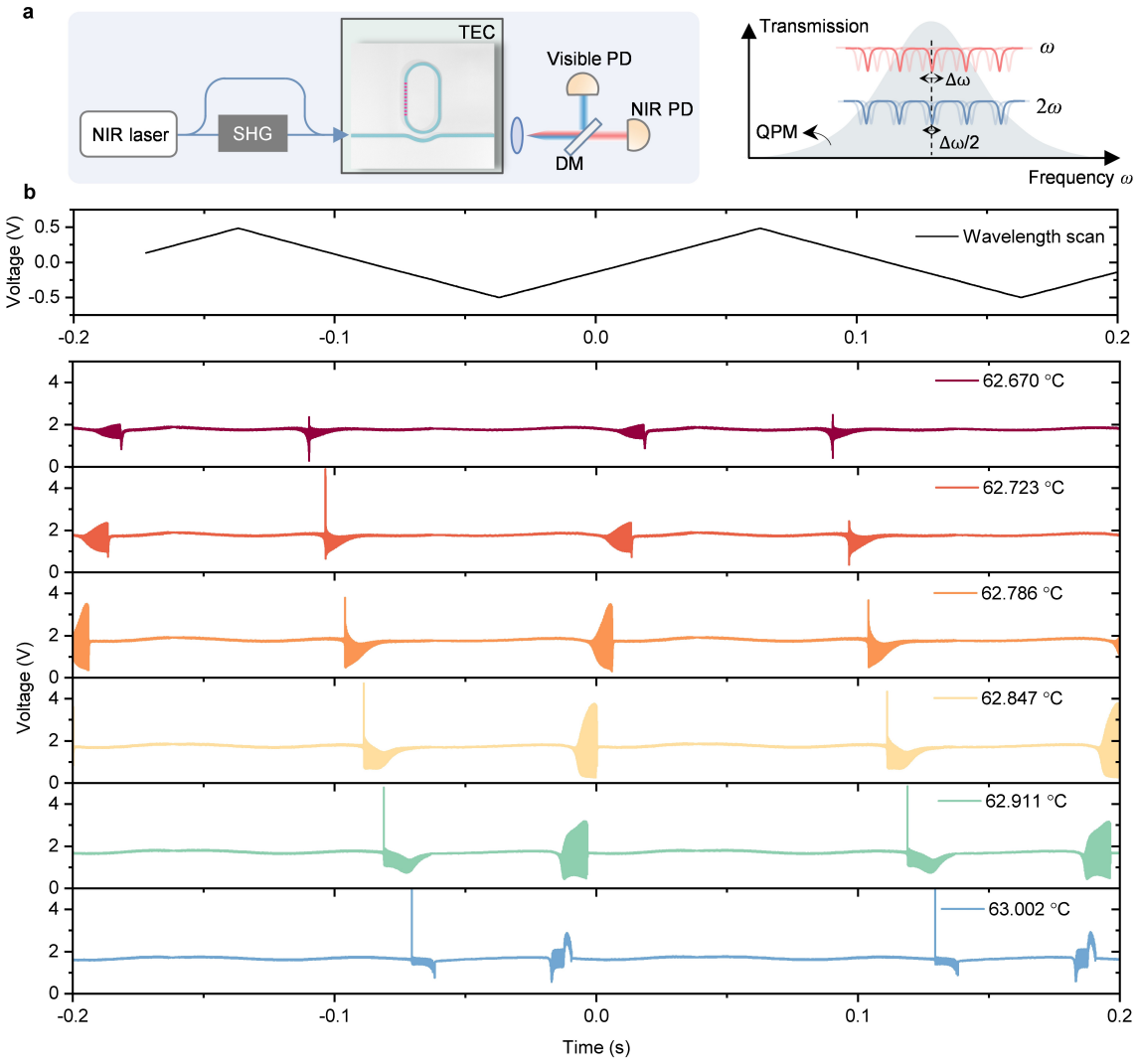

FIG. S2. **a**, Experimental setup for co-resonance measurement: a NIR seed and its SH generated by an external SHG module are injected into the device, and the transmissions of both modes are monitored while the chip temperature is tuned by a TEC. **b**, Conceptual illustration: the FH and SH resonances overlap within the QPM bandwidth. **c**, Transmission spectra of the two modes recorded at different temperatures, showing alternating amplification and de-amplification features when the resonances overlap.

V. Experimental setup for squeezing measurement

The squeezing measurement setup comprises a continuous-wave NIR laser serving as the local oscillator (LO), a SHG module using a bulk PPLN crystal to generate the visible pump field, and a high-quantum-efficiency balanced photodetector. The layout of the detection setup is shown in Fig. 4a. A 1587-nm CW laser is amplified to approximately 2 W using an L-band erbium-doped fiber amplifier, and the output is divided into two paths for SHG and LO generation. The SHG module provides the visible 793.5-nm pump photons that drive the $\chi^{(2)}$ interaction in the integrated squeezer, producing the squeezed vacuum field. The interferometer is symmetrized by carefully matching the optical path lengths of the squeezer and LO arms, which suppresses the conversion of laser-frequency noise into phase noise and enables stable quadrature measurements.

VI. Squeezing measurement for device 2

We also characterize a second device (device 2) with an escape efficiency of 85 %, accompanied by the relevant cavity and nonlinear calibrations necessary for accurate comparison.

A. Q-factor and escape efficiency characterization

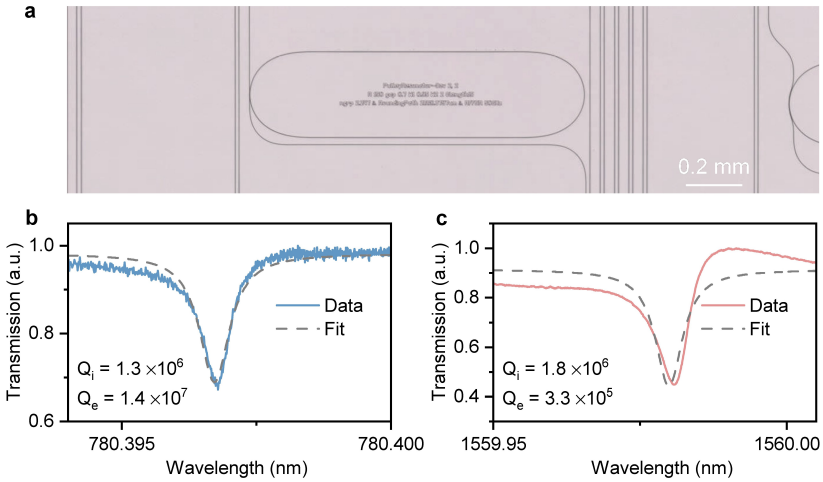

FIG. S3. Characterization of Device 2. **a**, Optical microscope image of the pulley-coupled microring with a 15 µm coupling length and 0.7 µm gap. Measured and fitted transmission spectrum of the visible **b** and telecom mode **c**, yielding quality factors of approximately $Q \approx 1.3 \times 10^6$ and 1.8×10^6, repectively. The device is undercoupled at visible and overcoupled at NIR, resulting in an escape efficiency of $\sim 85\%$ under the NIR coupling condition.

B. SHG and parametric emission characterization

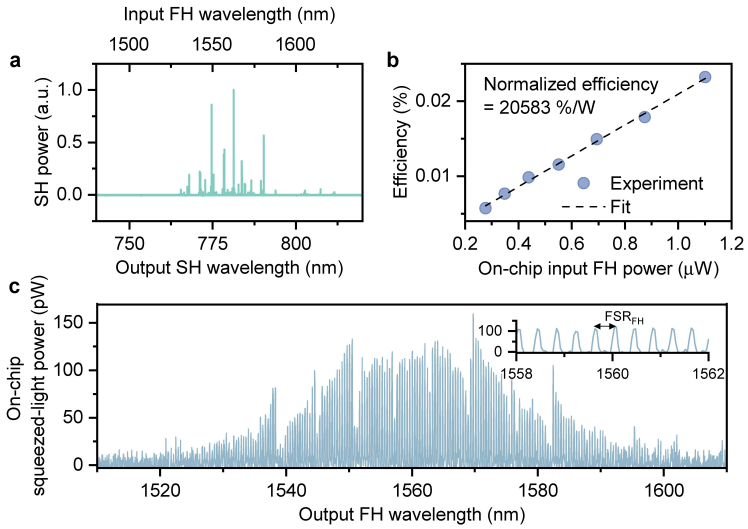

FIG. S4. Performance of SHG and parametric emission for the device with QPM near 1560 nm. **a**, Measured SHG spectrum showing a strong SH signal near 780 nm when the FH wavelength is tuned around 1560 nm. **b**, Normalized SHG efficiency extracted from the linear dependence of SH power on on-chip FH power, yielding 20 583 %/W. **c**, On-chip squeeezed light output spectrum as a function of FH wavelength, with a measured peak squeezeed light power of 110 pW. The inset shows the fine FSR features of the output spectrum which match with the resonator's FSR.

C. Squeezing measurement

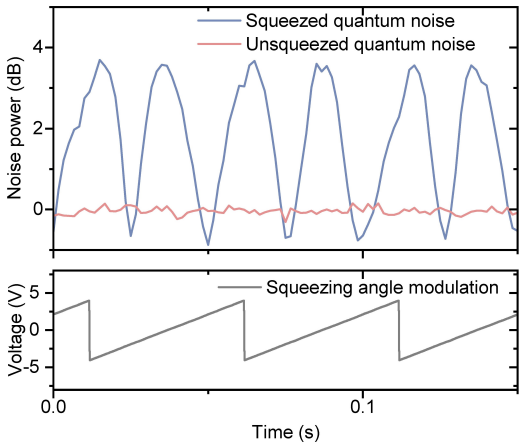

FIG. S5. Measured noise powers of the squeezed and antisqueezed quadratures as the squeezing angle is continuously modulated. The minimum noise level reaches −0.74 dB±0.08 dB of squeezing and the maximum reaches +3.58 dB±0.02 dB of anti-squeezing. The lower panel shows the applied phase-modulation voltage used to scan the squeezing angle.

D. Dependence of parametric gain and squeezing on pump detuning

We investigate the dependence of the parametric gain and the measured squeezing on the pump–cavity detuning. The pump wavelength is scanned relative to the cavity resonance, as illustrated schematically in Fig. S6(a). For each detuning point, the output squeezed light spectrum is recorded together with the squeezing and anti-squeezing traces obtained under phase scanning. Figure S6(b) shows the measured spectra for several pump detuning values around the resonance. When the pump is tuned close to zero detuning, the parametric gain is maximized. The corresponding squeezing traces are plotted in Fig. S6(c), where the blue and red curves represent the noise spectrum with squeezing angle modulation shot noise level, respectively. The maximum anti-squeezing and squeezing obtained at each detuning point are labeled on the right-hand side. As the pump approaches the cavity resonance, the measured anti-squeezing increases from approximately 0.9 dB to 3.2 dB, while the squeezing remains at a moderate level near −0.5 dB, limited by the detection loss. These trends confirm that the parametric gain is strongly dependent on the pump detuning, with the largest parametric amplification occurring when the pump is on resonance.

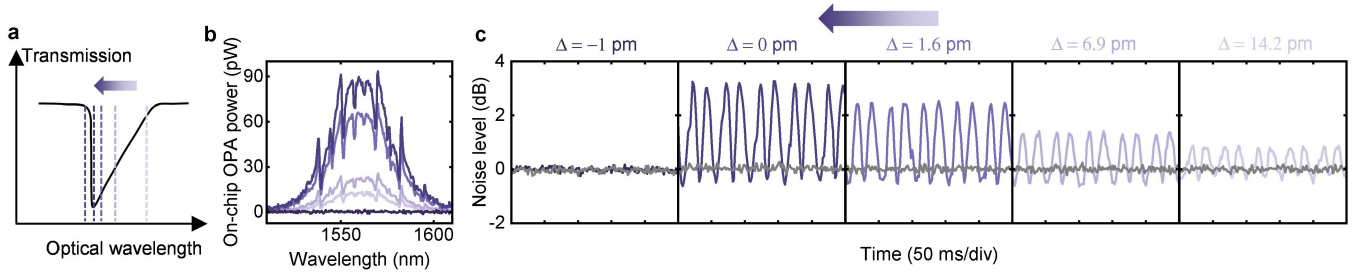

FIG. S6. Dependence of parametric gain and squeezing on pump detuning. **a**, Schematic of pump detuning relative to the cavity resonance. **b**, Measured spectra for several pump detuning values, showing maximum gain at zero detuning. **c**, Normalized noise spectrum and shot noise for different detuning conditions. Zero-detuning pumping results in the highest parametric gain and strongest quadrature modulation.

VII. Methods for inferring squeezing and threshold analysis

A. Inferred on-chip squeezing from loss tracking model

To infer the on-chip squeezing level in the output bus waveguide, we model the measured quadrature variances as a cascade of output facet transmission and effective off-chip transmission (including propagation loss, mode-overlap

visibility, and photodiode quantum efficiency).

The measured quadrature variances are related to the on-chip values by:

$$G_{\mathrm{mea},sqz} = \eta_{facet}\eta_{\mathrm{offchip}}G_{\mathrm{onchip},sqz} + 1 - \eta_{facet}\eta_{\mathrm{offchip}}, \tag{1}$$

$$G_{\mathrm{mea},asqz} = \eta_{facet}\eta_{\mathrm{offchip}}G_{\mathrm{onchip},asqz} + 1 - \eta_{facet}\eta_{\mathrm{offchip}}, \tag{2}$$

where η_{facet} denotes the output facet transmission efficiency.

The on-chip squeezing and anti-squeezing are connected to the intra-cavity (raw) quadrature variance through the escape efficiency η_{esc}:

$$G_{\mathrm{onchip},sqz} = \eta_{\mathrm{esc}}\frac{1}{G_{\mathrm{raw}}} + 1 - \eta_{\mathrm{esc}}, \tag{3}$$

$$G_{\mathrm{onchip},asqz} = \eta_{\mathrm{esc}}G_{\mathrm{raw}} + 1 - \eta_{\mathrm{esc}}. \tag{4}$$

These relations form a closed nonlinear system linking the measured noise levels to four unknown parameters. Using the calibrated efficiencies in Supplementary Table SI, we solve this system to determine

$$\begin{cases} \eta_{\mathrm{facet}} = 0.36 \quad (4.44\,\mathrm{dB}), \\ G_{\mathrm{onchip,sqz}} = 0.18 \quad (-7.52\,\mathrm{dB}), \\ G_{\mathrm{onchip,asqz}} = 9.15 \quad (+9.61\,\mathrm{dB}), \\ G_{\mathrm{raw}} = 9.90 \quad (9.96\,\mathrm{dB}) \end{cases} \tag{5}$$

for device 1. To estimate the uncertainty of the inferred on-chip squeezing and antisqueezing, we perform Monte Carlo uncertainty propagation. The measured known parameters (η_{esc}, η_{offchip}, measured squeezing $G_{\mathrm{mea},sqz}$ and anti-squeezing $G_{\mathrm{mea},asqz}$) are sampled according to their experimentally determined uncertainties. For each realization, the coupled nonlinear equations are solved to extract the corresponding output facet transmission and on-chip squeezing parameters. The resulting 1σ uncertainties are summarized in Supplementary Table SI.

The total detection efficiency η_{tot} in SI is obtained by multiplying the η_{facet} and effective off-chip transmission η_{offchip}, which refers only to the external loss channel after the cavity and does not include the escape efficiency η_{esc}. For device 1, this yields a total efficiency of

$$\eta_{\mathrm{tot}} = 20.7\%.$$

TABLE I. **Optical loss budget for the two devices' system and inferred on-chip squeezing.**

Device	Output facet loss (dB)	off-chip propagation loss (dB)	Visibility-induced loss (dB)	Quantum efficiency (dB)	Total loss η_{tot} (dB)	Escape efficiency	Measured squeezing/ anti-squeezing (dB)	On-chip squeezing/ anti-squeezing (dB)
Device 1 in main text	4.44 ±0.31 (36.0%)	1.45 ±0.2 (71.6%)	0.77 ±0.008 (91.5%^{2})	0.18 (96%)	6.84 (20.7%)	0.39 ±0.04 (91.5%)	-0.81 ±0.04 4.29 ±0.1	-7.52 ±0.22 9.62 ±0.25
Device 2 in SI	3.13 ±0.55 (48.6%)	0.40 ±0.2 (91.3%)	3.1 ±0.007 (70%^{2})	0.18 (96%)	6.81 (20.8%)	0.71 ±0.07 (85%)	-0.74 ±0.08 3.58 ±0.02	-5.96 ±0.27 8.53 ±0.43

Note: Uncertainties represent 1σ values obtained from Monte Carlo error propagation. Transmission efficiencies (shown in parentheses) are calculated from the mean dB values.

Supplementary Fig. S7 illustrates the relationship between total transmission efficiency and the expected measured squeezing/anti-squeezing for fixed on-chip values of $-7.52\,\mathrm{dB}$ and $+9.62\,\mathrm{dB}$. The star markers indicate the experimental operating point corresponding to $\eta_{\mathrm{tot}} \approx 0.2$, consistent with the loss budget and the above inference.

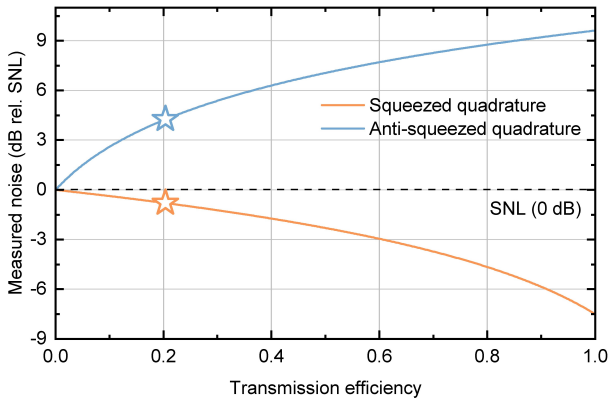

FIG. S7. Calculated squeezing and anti-squeezing levels as a function of total detection efficiency η, assuming an on-chip squeezing of $-7.52\,\mathrm{dB}$ and anti-squeezing of $+9.62\,\mathrm{dB}$. The star markers indicate the experimental operating point for device 1 at $\eta \approx 0.2$, corresponding to a measured squeezing of $-0.81\,\mathrm{dB}$ and anti-squeezing of $+4.29\,\mathrm{dB}$ relative to the shot-noise level (SNL).

B. Inferred squeezing from photon flux model

As a complementary cross-check, we infer the squeezing level from the measured on-chip squeezed-light power. For a degenerate phase-sensitive optical parametric amplifier seeded by vacuum, the mean photon number per temporal mode n inside the cavity is related to the squeezing parameter r via $n = \sinh^2 r$. The corresponding intra-cavity quadrature variances (normalized to the shot-noise level) are $G_{\mathrm{raw,sqz}} = e^{-2r}$ and $G_{\mathrm{raw,asqz}} = e^{+2r}$. Eliminating r yields

$$n = \frac{G_{\mathrm{raw,asqz}} + 1/G_{\mathrm{raw,asqz}} - 2}{4}, \tag{6}$$

which links the measured squeezed-light power to the intra-cavity quadrature variances.

For device 1, the intracavity power is obtained from the measured on-chip squeezed-light power $P_{\mathrm{sqz,on-chip}}$ by dividing by the escape efficiency η_{esc},

$$P_{\mathrm{cav}} = \frac{P_{\mathrm{sqz,on-chip}}}{\eta_{\mathrm{esc}}}. \tag{7}$$

Using the signal wavelength $\lambda \approx 1587.4\,\mathrm{nm}$ and the loaded cavity bandwidth B_{load}, the intracavity photon number per mode n is

$$n = \frac{P_{\mathrm{cav}}}{\hbar\omega B_{\mathrm{load}}}, \tag{8}$$

where $\omega = 2\pi c/\lambda$ is the optical angular frequency. Substituting n into the expression above yields the intra-cavity quadrature variances. To obtain realistic on-chip values, we incorporate the escape efficiency using the same loss model as in the loss-tracking analysis, and convert these variances back to dB.

$$G_{\mathrm{onchip,sqz}} = \eta_{\mathrm{esc}} G_{\mathrm{raw,sqz}} + (1 - \eta_{\mathrm{esc}}), \qquad G_{\mathrm{onchip,asqz}} = \eta_{\mathrm{esc}} G_{\mathrm{raw,asqz}} + (1 - \eta_{\mathrm{esc}}), \tag{9}$$

Using the parameters summarized in Supplementary Table SII ($P_{\mathrm{sqz,on-chip}} = 320\,\mathrm{pW}$, $\eta_{\mathrm{esc}} = 0.915$, and $B_{\mathrm{load}} = 1.36\,\mathrm{GHz}$), we obtain inferred on-chip squeezing and anti-squeezing levels of $-7.56\,\mathrm{dB}$ and $+9.70\,\mathrm{dB}$ for device 1. These values are consistent with those obtained from the loss-tracking model (Supplementary Table SI), supporting the reliability of the inferred on-chip performance.

C. Parametric oscillation threshold power ratio

Below-threshold operation of a degenerate $\chi^{(2)}$ optical parametric amplifier can be described using a normalized

TABLE II. **Inferred on-chip squeezing from photon flux model.**

Case	**Loaded linewidth** B_{load} **(MHz)**	**On-chip squeezed light power** $P_{sqz,on-chip}$**(pW)**	**Photon number flux** n **per Hz**	**Escape efficiency** η_{esc}**(%)**	**Measured squeezing/ anti-squeezing (dB)**	**On-chip squeezing/ anti-squeezing (dB)**
Device 1 in main text	1360	320	2.05	91.5	-0.81 / 4.29	-7.56 / 9.70
Device 2 in SI	690	120	1.61	85	-0.74 / 3.58	-5.98 / 8.58

pump power parameter

$$P_{\mathrm{ratio}} = \frac{P_{\mathrm{pump}}}{P_{\mathrm{th}}}, \tag{10}$$

where P_{pump} is the applied pump power at 2ω and P_{th} is the OPO threshold power. Thus, P_{ratio} represents the fraction of the oscillation threshold power at which the device is operated.

For $P_{\mathrm{ratio}} < 1$, squeezing and anti-squeezing rise smoothly with increasing pump power and diverge as the threshold is approached. The quadrature variances at sideband frequency f for a resonator with decay rate γ and effective detection efficiency ($\eta_{\mathrm{eff}} = \eta_{\mathrm{esc}}\eta_{\mathrm{tot}}$) are

$$V_{\mathrm{sqz}}(f) = 1 - \eta_{\mathrm{det}} \frac{4\sqrt{P_{\mathrm{ratio}}}}{\left(1+\sqrt{P_{\mathrm{ratio}}}\right)^2 + 4\left(2\pi f/\gamma\right)^2}, \tag{11}$$

$$V_{\mathrm{asqz}}(f) = 1 + \eta_{\mathrm{det}} \frac{4\sqrt{P_{\mathrm{ratio}}}}{\left(1-\sqrt{P_{\mathrm{ratio}}}\right)^2 + 4\left(2\pi f/\gamma\right)^2}. \tag{12}$$

Using the measured device parameters (loaded cavity bandwidth $B_{load} = \gamma/2\pi = 1.36\,\mathrm{GHz}$, escape efficiency $\eta_{\mathrm{esc}} = 0.915$, and total detection efficiency $\eta_{\mathrm{tot}} = 20.7\%$), the simulated spectra match the experimental results when

$$P_{\mathrm{ratio}} \approx 0.27. \tag{13}$$

This indicates operation at approximately 27.5 % of the parametric oscillation threshold. Increasing the visible pump power would raise P_{ratio} and allow stronger squeezing. This estimate agrees with the inferred on-chip squeezing and confirms the internal consistency of the device performance, while also indicating substantial headroom for improvement through reduced loss and better photorefractive and thermo-optic management.

VIII. Mitigation of the competition between photorefractive (PR) and thermo-optic (TO) effects in squeezer resonator

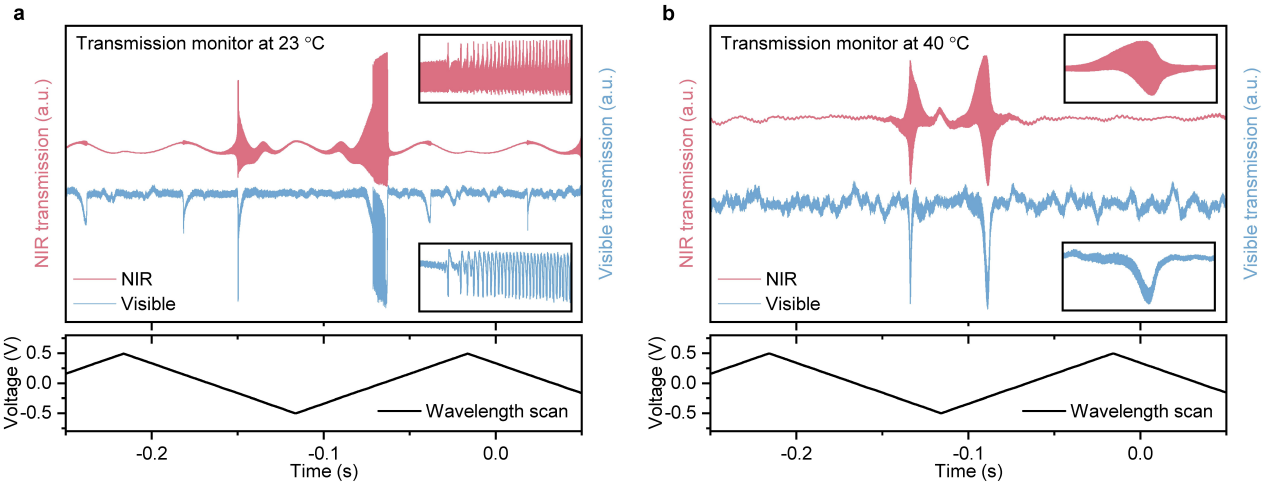

FIG. S8. Mitigation of photorefractive and thermo-optic competition at elevated temperature. Simultaneous transmission of the NIR (red) and visible (blue) modes is monitored during a wavelength scan at (left) 23 °C and (right) 40 °C. At 23 °C, strong PR/TO competition leads to pronounced, asymmetric amplitude fluctuations in both channels. At 40 °C, the traces remain smooth and stable, demonstrating that PR/TO competition is effectively suppressed at higher temperature under comparable pump power.